JOURNAL OF GEOPHYSICAL RESEARCH, VOL. 106, NO. C9, PAGES 19,611–19,623, SEPTEMBER 15, 2001

A numerical study of the upwelling circulation off central Chile

Jorge M. Mesias,[1] Ricardo P. Matano, and P. Ted Strub

College of Oceanic and Atmospheric Sciences, Oregon State University, Corvallis, Oregon, USA

Abstract. We present a modeling study of the upwelling ocean circulation off central Chile (34°-40°S). Using a primitive equation model, we make a numerical simulation of the ocean circulation for summer of 1993, a year characterized by moderate but persistent equatorward winds. The results indicate the formation of an eastern boundary current system that shows classical Ekman and geostrophic dynamics. A strong equatorward coastal jet develops during intense upwelling activity, induced by the prevailing equatorward winds. The spatial and temporal variability of the upwelling-favorable winds strongly controls the variability in the oceanic circulation. Upwelling activity in the coastal areas occurs during periods of growth, peak, and decay. The circulation in the region is divided into two distinct dynamical areas that extend north and south of a prominent cape (Punta Lavapie), located in the center of the model domain. During the peak upwelling stage, the equatorward jet separates from the coast at Punta Lavapie and remains separated in the northern region. This detachment is followed by the formation of cyclonic eddies and decreased upwelling during periods of wind relaxation. The northern area is affected by advection processes and weaker local winds. In contrast, the equatorward flows in the southern region are persistently attached to the coastline and are more coherent with the stronger local winds.

1. Introduction

The ocean currents along the central Chilean coast (34°-40°S, Figure 1) form part of the Peru-Chile Current System, whose main features are (1) the surface Chile Coastal Current (CCC), which is found in the upper 100 m of the ocean in the limit between the continental slope and shelf, flows equatorward during the summer, and reverses during the winter; (2) the (Gunther) Poleward Undercurrent (PUC), which flows below the CCC at depths of 150-400 m [*Nuñez,* 1996] and has unknown seasonality; and (3) the poleward surface Peru-Chile Countercurrent (PCCC), which flows 100-300 km offshore in the upper 100 m between ~6° and 40°S and has maximum velocities in austral spring and minima in fall [*Strub et al.,* 1995, 1998]. Although the southward extension of the PCCC current into the Gulf of Arauco area (37°S) is not certain [*Strub et al.,* 1995; *Nuñez,* 1996], we include it for completeness. Figure 1a shows a cartoon illustration of the summer circulation in the region, depicting a limited southward intrusion of the PCCC and oceanic and coastal branches of the CCC current.

The winds along the central Chilean coast are influenced by the seasonal displacement of the Subtropical Anticyclone of the southeast Pacific (atmospheric high-pressure system) and the passing of synoptic disturbances [*Djurdfeldt,* 1989; *Rutllant,* 1993]. During summer they are predominantly equatorward, inducing intense and persistent upwelling activity from 35° to 38°S, which is characterized by the offshore extension (up to 150 km) of plumes of cold water. The intensity of the upwelling fluctuates during episodes of wind relaxation or strong southward bursts [*Caceres and Arcos,* 1991]. Estimations of Ekman transport indices indicate that cold waters are upwelled from 150 to 200 m depth, with timescales of the order of 2-7 days [*Arcos and Navarro,* 1986]. Observations show that the alongshore component of the currents correlates well with the wind speed, at a time lag of 18-36 hours, which is comparable to the 20 hour local inertial period [*Ahumada,* 1989]. During some years the intensity of the local winds is affected by a weakening of the atmospheric high-pressure system (centered around Eastern Island) and by a strenghthening of a low-pressure cell centered near Australia [*Ramage,* 1986]. These Southern Oscillation events are typical of the development of El Niño at midlatitudes off South America [*Rutllant,* 1993].

The upwelling regime along the central Chilean coast was studied by *Vergara* [1991, 1993], using a two-layer

[1]Now at the School for Marine Science and Technology, University of Massachusetts Dartmouth, New Bedford, Massachusetts, USA.

Paper number 2000JC000649.
0148-0227/01/2000JC000649$09.00

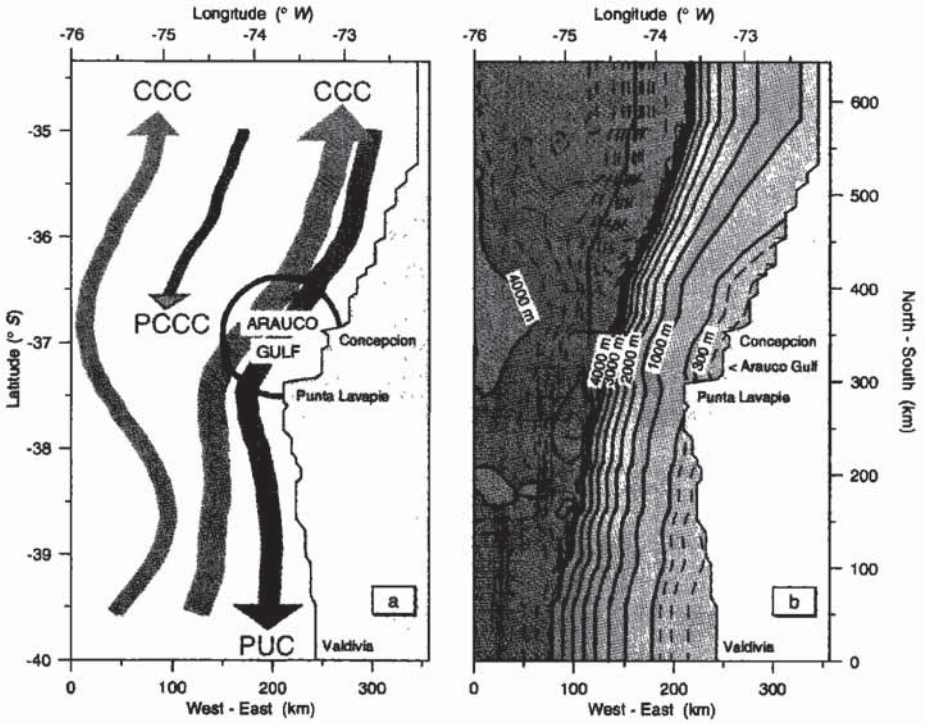

Figure 1. (a) Cartoon of observed large-scale coastal currents in the region during austral summer: the Chile Coastal Current (CCC), the Peru-Chile Countercurrent (PCCC), and the Poleward Undercurrent (PUC). (b) Bottom topography (in m) of the model domain.

shallow water model. These model experiments found that the geometry of the coastline (around the Gulf of Arauco) leads to enhanced upwelling activity. *Shaffer et al.* [1995, 1997] found that locally generated upwelling at 30°S is modulated by distantly forced coastal trapped waves with periods of ~50 days, originating along the equator. *Clark and Ahmed* [1999] modeled the southward propagation of equatorial oscillations with periods of 1-2 months and speeds of 250 km d^{-1}. Their model predicted the presence of a coastal subsurface equatorward current that is trapped along the upper continental slope. These predictions are partially in agreement with current meter observations at 30°S [*Shaffer et al.*, 1995, 1997]. Other numerical efforts to study the circulation off the Chilean coast have not focused on the region of our interest [*Batteen et al.*, 1995] or have used outputs of larger-scale circulation models without examining the dynamics of coastal upwelling itself [*Nuñez*, 1996].

The objective of this study is to investigate the upwelling regime in the region centered around the Gulf of Arauco. In particular, we would like to characterize (1) the summertime ocean circulation, (2) the effects of the bottom topography and coastline geometry on the upwelling regime, and (3) the oceanic variability caused by differences between years with weak and strong atmospheric wind forcing. To address these issues, we conduct a series of numerical experiments using the Princeton Ocean Model (POM). The model includes a realistic coastline and bottom topography and is forced with daily wind stress fields corresponding to the austral summer of 1993. These stresses are derived from data sets of the European Centre for Medium-Range Weather Forecasts. The experiments are initialized with annual climatological temperature and salinity fields [*Levitus and Gelfeld*, 1992]. Heat and salt surface fluxes are simulated by restoring the surface layer to monthly climatological values of temperature and salinity.

In this article we analyze the results of a benchmark simulation forced with the 1993 wind fields. This year of moderate wind intensity is chosen to characterize the average summertime circulation along the Chilean coast and to identify effects of the bottom topography and coastline geometry on the upwelling dynamics. Further analyses on (1) the flow dynamics for this benchmark experiment, using its momentum and vorticity balances, and (2) the effects of interannual changes in wind forcing, using experiments with weaker (1992) and stronger winds (1994), will be described in a future article.

In section 2 we offer a brief description of the numerical model and surface atmospheric forcing fields. In section 3 we present the results of our benchmark experiment. In section 4 we summarize and discuss the results.

2. Model and Experiments

POM is a three-dimensional, nonlinear primitive equation coastal ocean circulation model. It includes a free surface and uses a σ coordinate transformation

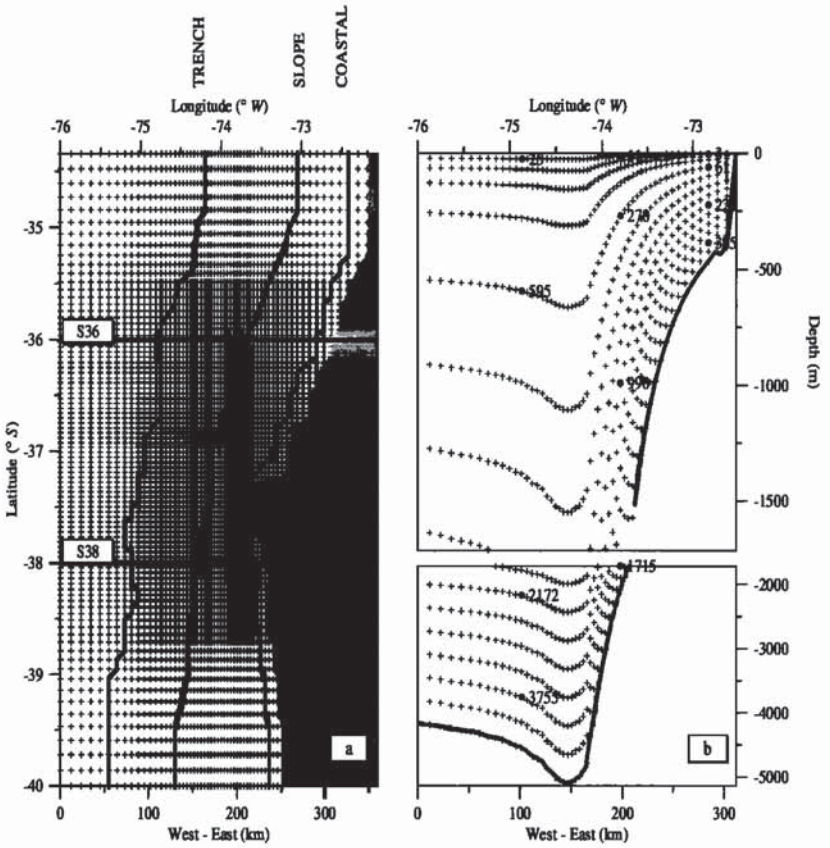

Figure 2. (a) Horizontal model grid (shaded crosses). Dark lines correspond to sections used for the analysis of the model outputs. (b) Vertical model grid (shaded crosses) at cross- section S36. Note the change in scale at -1750 m. Solid dots indicate the depth (in m) of the σ levels K=1,5,9, and 13 used during the analyses of the model outputs.

that scales the size of each vertical level to the water depth. The coefficients of horizontal mixing are calculated using Smagorinski's formulation [*Smagorinski,* 1963], while the coefficients of vertical mixing follow a second-order turbulence closure scheme [*Mellor and Yamada,* 1982]. POM uses a split mode time step that solves the vertically integrated equations (external mode) separately from the equations for deviations from the external mode at each of the model levels (internal mode). A detailed description of the model is given by *Blumberg and Mellor* [1987].

Figure 1b shows the domain of our experiment. The bottom topography was smoothed to comply with the constraints introduced by the use of the σ coordinates [*Mellor et al.,* 1994]. The two main topographical features in the region are (1) the Gulf of Arauco and the Punta Lavapie cape, which mark an inflexion of the coastline, and (2) the Peru-Chile Trench, which rapidly deepens as the continental slope drops from 500 to ~5500 m depth. The trench is deeper in the north. The model was initialized with climatological temperature and salinity values [*Levitus and Gelfeld,* 1992]. The horizontal resolution ranges from 3.5 km near the coast to 13 km farther offshore (Figure 2a), while the vertical axis is discretized in 15 σ levels with higher resolution in the upper ocean (Figure 2b). Tests with 30 σ levels produced small differences and greatly increased run time.

2.1. Boundary Conditions

The northern, southern, and western borders of our model region are open. At those boundaries we implement different open boundary conditions (OBC) for the external and internal modes. For the external mode, the northern and southern boundary conditions are a combination of radiation and continuity conditions plus a "local solution approach." The sea surface height is updated with a gravity wave radiation condition, while the barotropic normal velocities are calculated as $U = U_o + \sqrt{g/H}(\eta - \eta_o)$. U_o and η_o are prescribed values determined by solving a linearized set of the model equations that do not include normal derivatives and do not need an OBC. A detailed account of the OBC conditions for the external mode is given by *Palma and Matano* [1998].

For the internal mode, baroclinic normal velocity, temperature, and salinity variables at the northern and southern boundaries are specified using a combination of advection plus Orlanski's radiation conditions: $\phi_t + (C + u)\phi_x = 0$, where ϕ represents any of the inter-

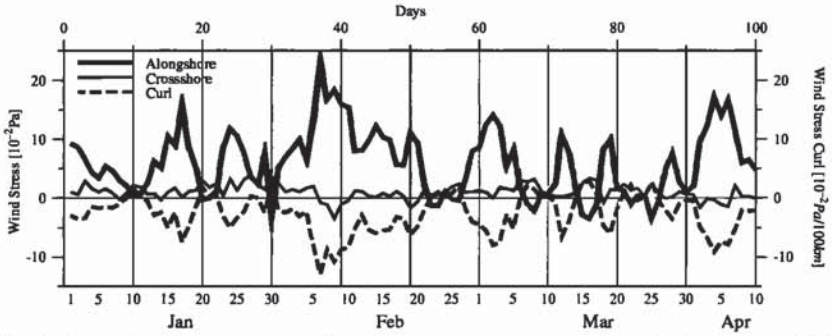

Figure 3. Evolution of area-averaged wind stress components and wind stress curl fields during the benchmark experiment (summer of 1993). Positive values indicate winds toward the north and east and anticyclonic curl.

nal variables, C is the phase speed of the propagating waves, and u is the internal normal velocity. Tangential barotropic and baroclinic velocities are determined using a zero gradient condition.

At the western border, all the external and internal fields are clamped in combination with a relaxation scheme that ensures a continuous change toward the interior domain. The "clamping" of western variables is supported by the fact that the transport of physical properties into the region from the west is negligible compared with those at the northern and southern boundaries. The combined OBC conditions for the external and internal fields have been succesfully used in a variety of idealized and realistic tests, including the domain of the central part of the Chilean coast [*Matano et al.*, 1998].

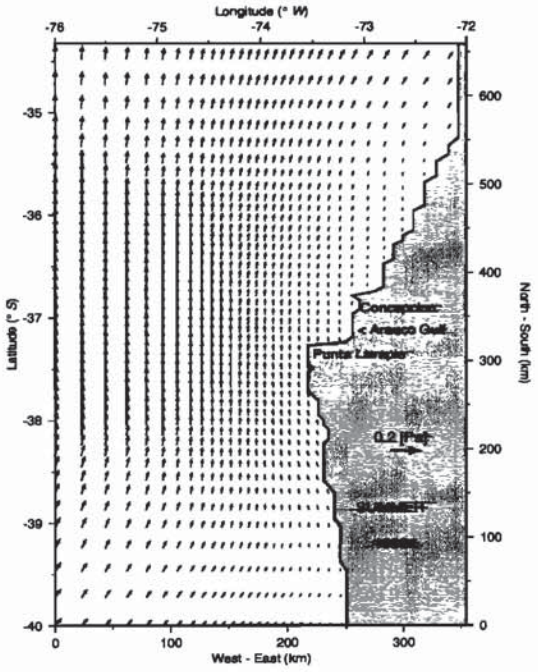

Figure 4. Mean wind stress field of the benchmark experiment.

2.2. Surface Forcing

The model is forced with wind stress fields corresponding to the summer of 1993. These stresses are derived from twice-daily wind speeds calculated at the European Centre for Medium-Range Weather Forecasts (ECMWF) on a global 2.5°×2.5° grid [*Lonnberg et al.*, 1989]. The eastward (τ_x) and northward (τ_y) wind stress components are calculated using a bulk aerodynamic formula with drag coefficients estimated according to *Trenberth et al.* [1989]. The computed daily wind stress fields are then interpolated onto the horizontal model grid and linearly interpolated at each external time step during the numerical experiments.

The surface heat and salt fluxes are simulated by a relaxation of the temperature and salinity values to their monthly climatology [*Levitus and Gelfeld*, 1992], using the formula $T^{n+1} = T^n - (\delta t/\alpha)(T^n - T^n{}_L)$. Here T^n represents the model surface temperature or salinity variable at time n, $T^n{}_L$ is the corresponding temporally interpolated Levitus variable at time n, δt is the time interval, and α is the restoring timescale, which is 30 days.

3. Benchmark Experiment

The experiment is started from rest on January 1 of 1993 and run for a period of 100 days. To avoid the forcing of inertial oscillations, we ramp the winds during a 20 hour local inertial period. The time steps used in our experiment are of 6.4 and 192.5 s for the external and internal modes, calculated accordingly to the Courant-Friedrichs-Levy (CFL) stability conditions.

In Figures 3 and 4 we show the temporal evolution and the spatial pattern of the summertime mean wind stress forcing. Intense events of equatorward (positive) winds, with cyclonic (negative) curl, dominate the summer period, reaching a maximum during February when the Subtropical Anticyclone is at its southernmost location. The periods of these events range from 3 to 15 days, alternating with short episodes (1-4 days) of weakened or reversed (southward) winds that become more frequent as the autumn season approaches.

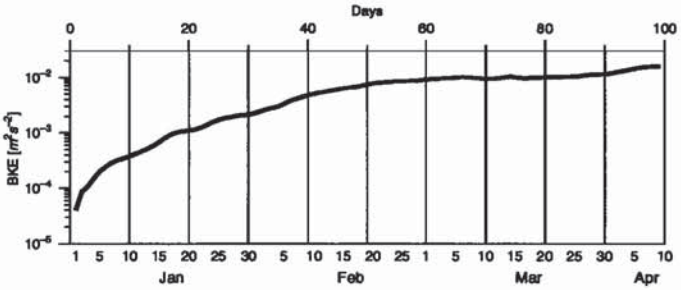

Figure 5. Volume-averaged barotropic kinetic energy (BKE) for the benchmark experiment.

Although the stress field shown in Figure 4 is mostly dominated by an equatorward wind component, there are marked regional differences in wind strength. Over the coastal areas, for example, the winds are weaker than over the offshore regions. South of Punta Lavapie the coastal winds are stronger and fluctuate (in time) more than in the northern coastal areas (not shown). In the north the coastal equatorward winds are not as strong but tend to persist during the entire summer. The corresponding summertime wind stress curl map (not shown) indicates that negative (cyclonic) wind stress curl dominates over the entire area, being particularly strong near Punta Lavapie.

To illustrate the oceanic adjustment to the atmospheric forcing, Figure 5 shows the temporal evolution of the domain-averaged barotropic kinetic energy. Dur-

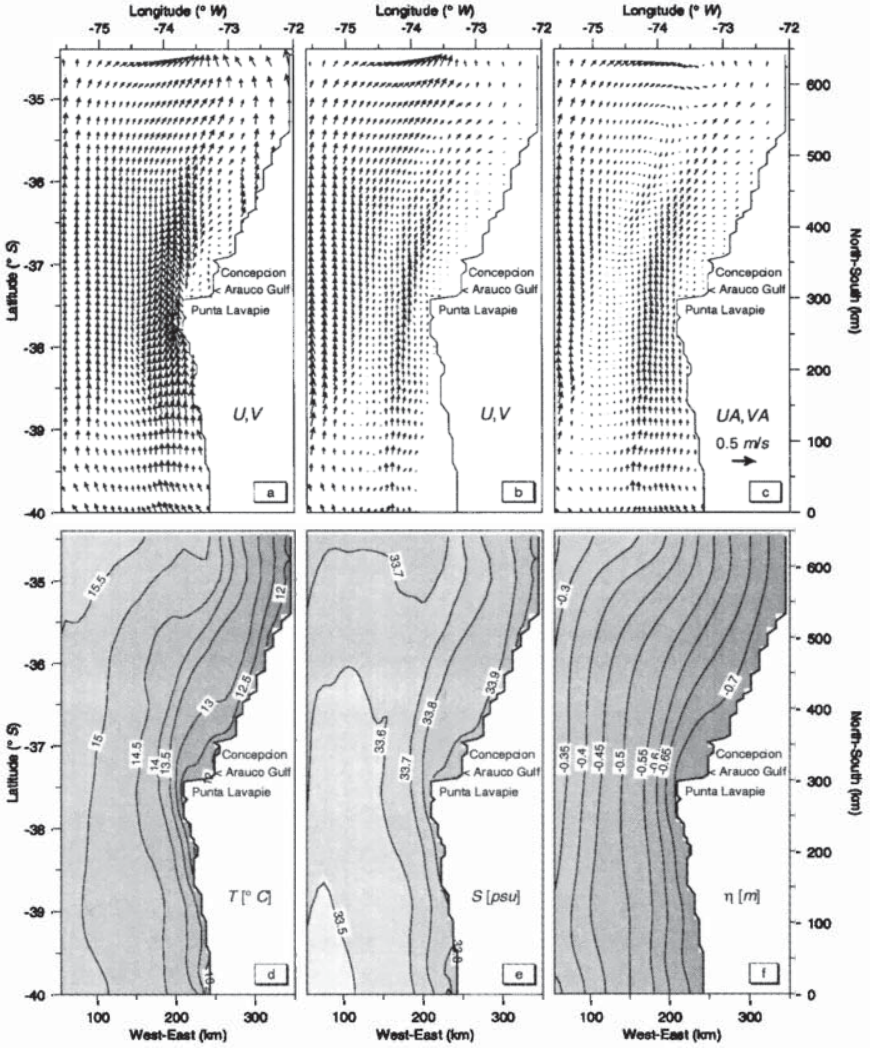

Figure 6. Maps of time-averaged (last 50 simulation days) model fields from the benchmark experiment. Depicted fields are (a) surface velocity, (b) velocity at 350 m depth, (c) depth-averaged velocity, (d) surface temperature, (e) surface salinity, and (f) surface height. Darker shading corresponds to water that is colder, saltier, and lower in height.

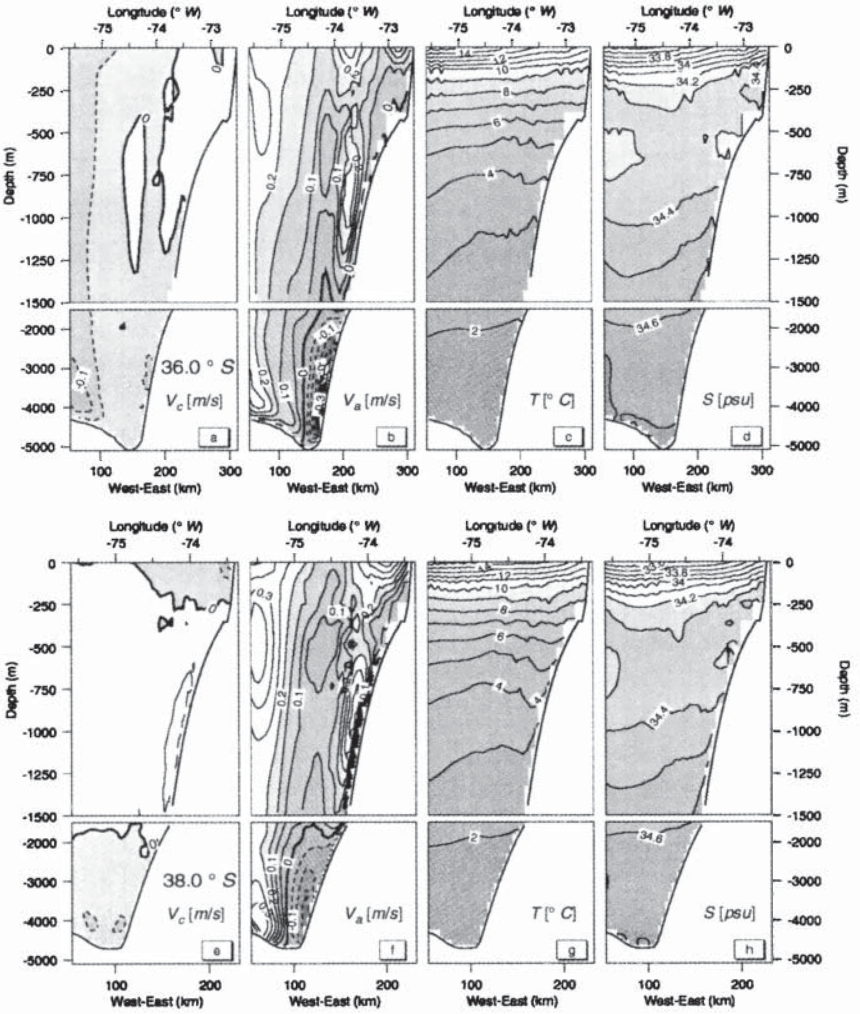

Figure 7. Zonal sections at (top) 36°S and (bottom) 38°S of time-averaged (last 50 simulation days) model fields from the benchmark experiment. From left to right are depicted fields of cross-shore velocity V_c, alongshore velocity V_a, temperature T, and salinity S. The contour intervals for V_c and V_a are 0.05 m s^{-1}. Dark shading indicates westward velocities, southward velocities, and northward velocities <0.2 m s^{-1}, colder water, and saltier water, respectively.

ing the first 15 days of the spin up process the kinetic energy increases steadily, as the flow adjusts its density structure to the wind stress forcing and bottom topography. After day 25, the model fields are largely affected by energy inputs from the wind stress and heat/salt surface fluxes. The largest energy inputs occur during periods of intense equatorward wind events, which reach their peak by day 50. After that, the kinetic energy remains relatively constant.

3.1. Mean Fields

The climatological averages of the model variables are presented in Figures 6 and 7. These averages are calculated over the last 50 simulation days. The circulation shows a system of currents that is qualitatively similar to the cartoon in Figure 1a. The model ocean currents consist of (1) a strong surface coastal jet (Figure 6a), identifiable with the known CCC current, flowing above 100 m over the continental shelf and slope (Figures 7b and 7f), which lie north and south of the Gulf of Arauco and Concepcion Bay areas; (2) a weak poleward subsurface current (Figures 7b and 7d), identifiable with the known PUC countercurrent, flowing over the shelf and upper slope and below the CCC at depths of 200-500 m; (3) an offshore surface equatorward current (Figures 6a and 6b, west of ~75°W), identifiable as the oceanic branch of the CCC, with a deep and broad core at 300-600 m depth (Figures 7b and 7f) which is separated from the coastal branch by a narrow region of weak surface flows located along the axis of the Peru-Chile trench; (4) a strong subsurface equatorward current, similar to previously observed flows, whose core is located over the upper slope at ~1000 m depth (Figures 7b and 7f) and dominates the depth-integrated currents (Figure 6c, along the 74°-73°W meridians) and which has been called the Subsurface Chile Coastal Current (SCCC); (5) a deep and strong poleward current (bottom insert of Figures 7b and 7f), not previously

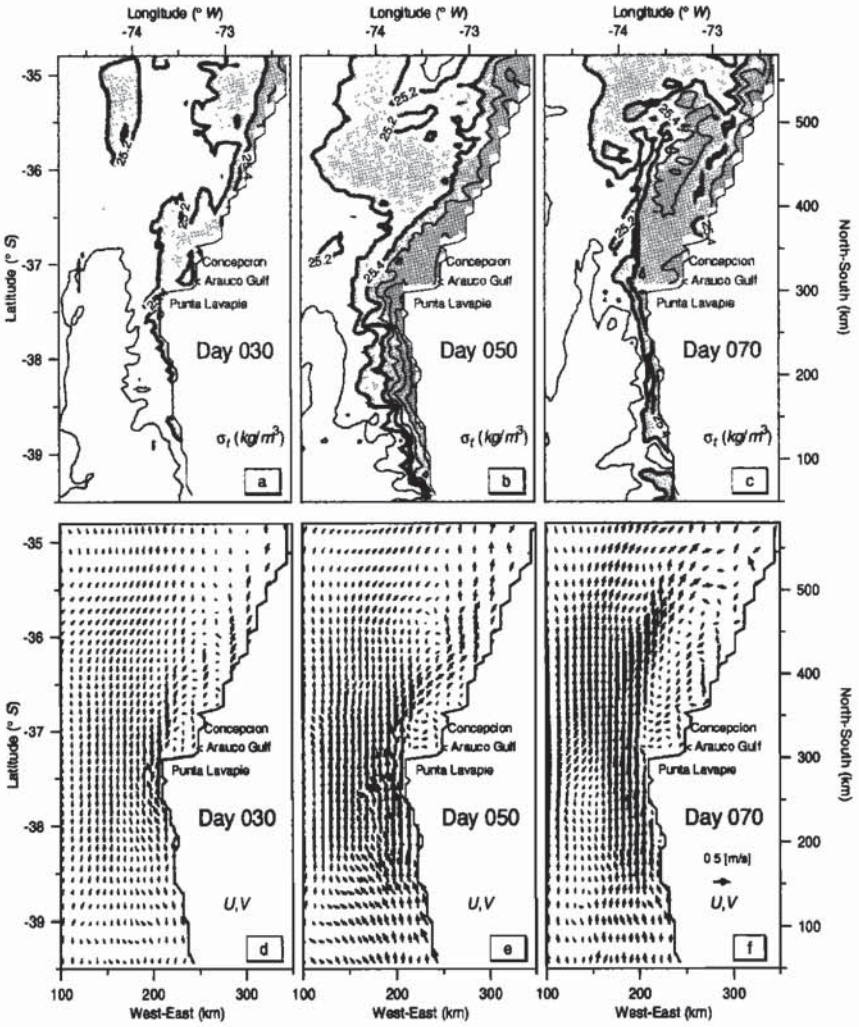

Figure 8. Snapshots every 20 days of surface density σ_t and surface velocity (U, V) fields of the benchmark experiment. Offshore distances of thickened isopycnals 25.2 and 25.4 kg m^{-3} are dynamically related to the coastal jet. Dark shading indicates denser water.

named, flowing on the inshore side of the PCT trench, below the region of weak surface flows, which is referred to as the Deep Poleward Current (DPC).

The area separating the oceanic and coastal branches of the surface CCC current roughly corresponds to the location of the PCCC countercurrent [*Strub et al.*, 1995, 1998; *Nuñez*, 1996], which is not observed here. However, this region of weak surface flows (seemingly induced by the presence of the deep Peru-Chile Trench) could eventually facilitate the southward intrusion of the PCCC countercurrent that forms farther north. The SCCC current is similar to that predicted by *Clark and Ahmed* [1999], and its existence has been partially confirmed by current meter observations made at 30°S by *Shaffer et al.* [1995, 1997], although with lower strengths. Our predicted DPC current has been observed by *Shaffer et al.* [1995], but they suggested that it extends downward only to 3400 m deep, flowing over an abyssal equatorward current originating through deep internal mixing activity. In contrast, the model DPC countercurrent here extends well inside the Peru-Chile Trench. There are no observations to check the existence of the SCCC and DPC currents in the Gulf of Arauco region. However, the apparent realism of the upper circulation suggests that they are plausible components of the deep ocean circulation in the area.

The mean surface fields in Figures 6d-6f show the persistence of cold and salty waters along the coast and a steep downward tilting of the ocean surface toward the coast in response to the formation of a geostrophic coastal equatorward (CCC) jet (Figures 7b and 7f). The coastal upwelling activity is forced by the offshore Ekman transport (see Figures 7a and 7f) generated by the prevailing equatorward winds; it is also enhanced in its offshore extension by the dominant cyclonic wind stress curl via "Ekman pumping" [*Enriquez and Friehe*, 1995]. The vertical sections of temperature and salinity in Figures 7c, 7d, 7g and 7h indicate that these denser waters upwell onto the continental shelf from ~200 to 500 m depths. In the coastal areas the up-

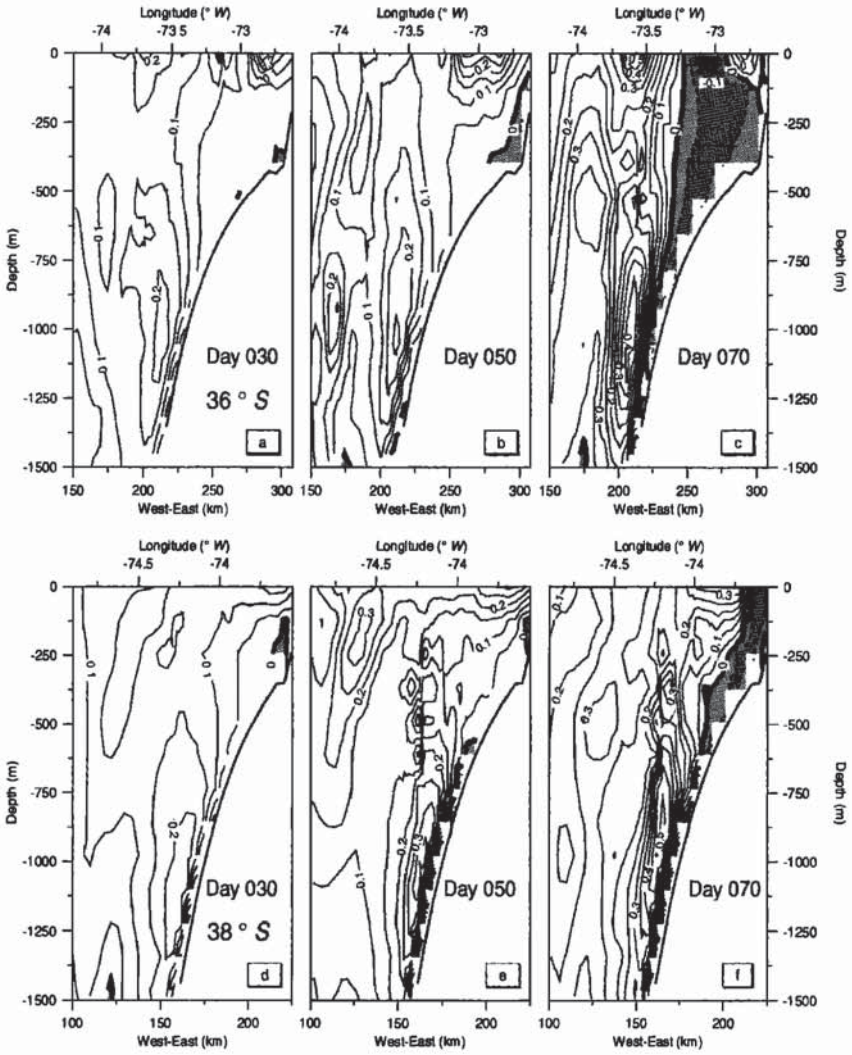

Figure 9. Zonal sections of alongshore velocity (in m s^{-1}) at latitudes 36° and 38°S for days 30, 50, and 70 of the benchmark experiment. The contour interval is 0.05 m s^{-1}, and darker shading denotes poleward alongshore flows.

welling of colder waters causes the ocean to gain much more heat than it would without upwelling (through latent, sensible, and infrared heat fluxes). The inclusion of heat/salt fluxes (simulated with the Newtonian restoring) decreases the offshore extent of lower sea surface temperature (SST) values and makes the ocean more stratified than if heating were not included.

3.2. Upwelling

In this section we analyze the temporal and spatial variability of the upwelling activity that results from the evolving wind stress forcing. To illustrate the time evolution of the upwelling regime we selected snapshots of days that characterize the periods of growth (day 30), peak (day 50), and decay (day 70). The snapshots are complemented by spectral analysis of local time series at different locations.

3.2.1. Growth. The midpoint of the growth stage is reached after two episodes of moderate equatorward winds occurred centered at days 15 and 25 (Figure 3). This stage lasts until approximately day 35 when the upwelling-favorable winds strongly increase (Figure 3). Figure 8a shows the development of an upwelling front whose offshore extension varies along the coast, as indicated by the location of the 25.2 and 25.4 kg m^{-3} isopycnals. These isopycnals coincide with the 14° and 13°C isotherms.

South of Punta Lavapie the surface velocity field corresponding to day 30 shows a coastal jet that reaches a maximum speed of ~0.2 m s^{-1} and closely follows the coastline geometry with small-scale meanderings (Figure 8d). Below this surface coastal jet, which extends downward up to 100 m (Figure 9d), there is a poleward countercurrent with speeds <0.05 m s^{-1}. Immediately after passing Punta Lavapie, the equatorward coastal jet forms a cyclonic eddy in the Gulf of Arauco of ~30 km diameter, approximately the crosshore width of the gulf (Figure 8d).

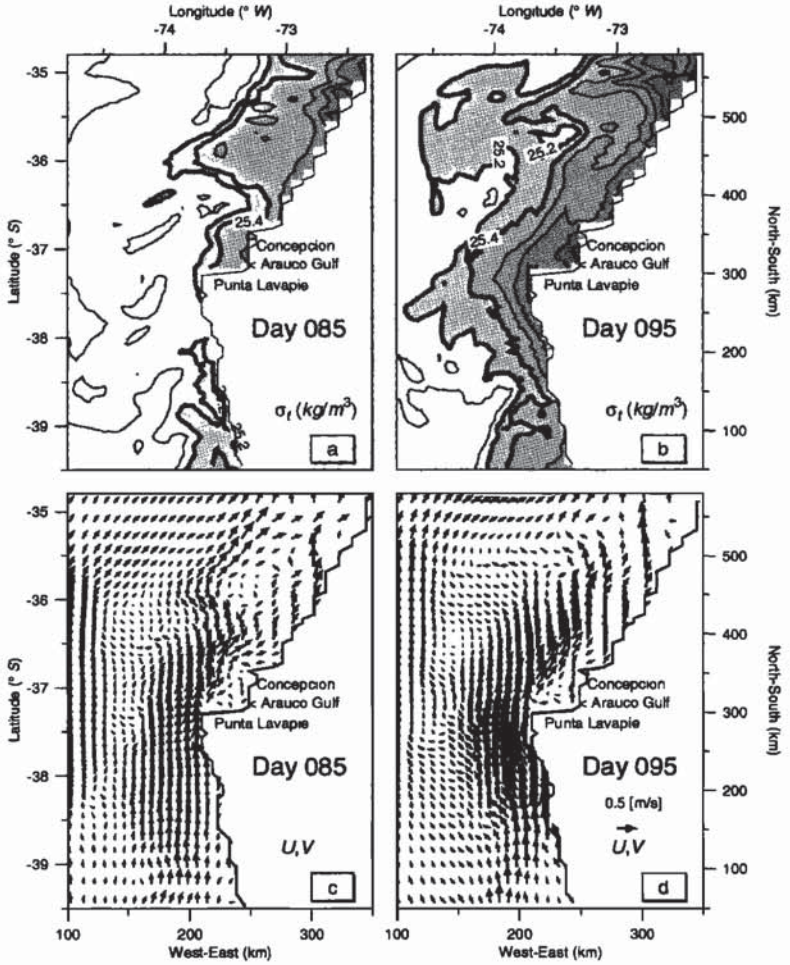

Figure 10. Snapshots at days 85 and 95 of surface density σ_t and surface velocity (U, V) fields of the benchmark experiment.

In the northern areas the surface coastal jet reaches a maximum speed of ~0.3 m s^{-1} (Figure 9a), larger than in the southern areas, flowing over a weaker poleward countercurrent. On the offshore side of the continental shelf the coastal equatorward jet decreases in intensity over the slope, especially in the northernmost region where the Peru-Chile Trench significantly and rapidly deepens by 1000 m.

3.2.2. Peak. The upwelling activity reaches its peak at approximately day 50, which corresponds to the end of the longest and strongest episode of equatorward winds (Figure 3a). The location of the 25.2 kg m^{-3} isopycnal in Figure 8b shows the displacement of the front to ~50 km at Punta Lavapie and over ~100 km offshore north of 36°S. Owing to the influence of the coastline [*Vergara*, 1993] and the strong local alongshore winds (see Figure 4) the front becomes particularly strong south of Punta Lavapie, where deeper waters are carried upward. In this region the surface coastal jet (Figures 8e and 9e) is very strong (up to ~0.4 m s^{-1}) and broad (reaching ~50-80 km width), closely following the coastline as it moves northward until Punta Lavapie, where it separates from the coast. In the region around 38°S (Figure 9e) the poleward subsurface countercurrent is relatively weak (<0.05 m s^{-1}) and separates into an upper part that flows over the 250 m isobath and a deeper part flowing between the 600 and 1000 m isobaths over the slope.

North of Punta Lavapie the frontal zone is more diffuse until the jet passes Concepcion Bay and returns to the coast approximately at 36°S (Figures 8b and 8e). North of Concepcion Bay the equatorward coastal jet (Figure 9b) reaches a maximum speed of ~0.5 m s^{-1} and extends downward to ~200 m. Flowing below and onshore of the jet, the poleward countercurrent is stronger with a maximum speed of ~0.05 m s^{-1} and extends over most of the continental shelf and upper slope.

3.2.3. Decay. The transition to downwelling conditions is favored by the relaxation of the equatorward winds and the passage of weak or moderate cyclonic atmospheric disturbances of ~4 day periods. At day 70, Figure 8c shows a decrease of the upwelling activity characterized by movement of the 25.4 kg m^{-3} isopycnal toward the coast in the southern region and by an onshore and southward intrusion of lighter water over the

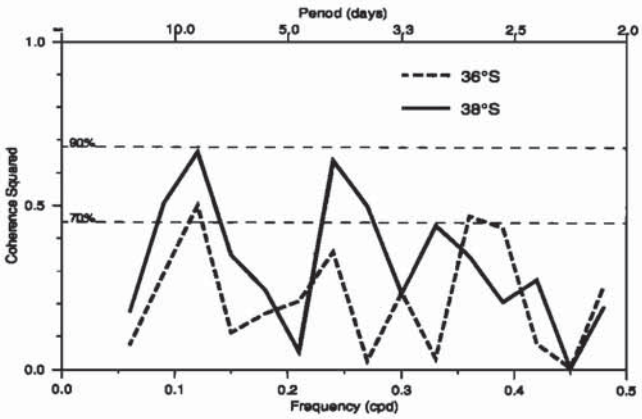

Figure 11. Coherence between series of alongshore components of local wind stress and surface velocity fields. Ocean fields are from "coastal" locations, and calculations were made with six degrees of freedom.

inshore northern region (along ~73°W between 37° and 35.5°S). This southward intrusion signals the presence of a cyclonic eddy that initially forms inside the Gulf of Arauco (37°S) and extends north to latitude 35.5°S (Figure 8f). During the formation of the cyclonic eddy its northern edge moves northward at a rate of ~10 km d^{-1}. North of 35.5°S the eddy growth is arrested by persistently equatorward winds. By day 70, Figures 8f and 9c show the development of a narrow equatorward surface current between the coastline and the cyclonic eddy, whose poleward branch extends downward over the entire continental shelf. The narrow equatorward current forms from a retroflection of the poleward flow of the cyclonic eddy after encountering the Gulf of Arauco (Figure 8f), a process favored by the westward displacement of the eddy itself and a period of moderate equatorward wind that occurs between days 55 and 65. Inside the Gulf of Arauco and Concepcion Bay the current retroflection appears as anticyclonic eddies filling the Gulf and the Bay.

The eddy activity in the northern coastal region generates a complex system of alternating equatorward and poleward currents that extend from surface to bottom (Figure 9c). These currents strongly interact, as they are affected by alternating equatorward and poleward winds. The zonal sections in Figure 9 shows that the alongshore currents at day 70 are more intense than those at day 50, a difference that extends all along the coast and can also be observed in the plots of surface currents shown in Figure 8. The progressive intensification of the ocean currents is a result of the overall dominance of the equatorward winds during the entire summertime period (Figure 3a).

At day 70 the zonal sections of alongshore flow in Figure 9 also show a subsurface equatorward current with its core centered at ~1000 m depth and over the slope. This fluctuating subsurface current is trapped along the upper continental slope during the entire simulation, similar to that predicted in the study by *Clark and Ahmed* [1999] at 35°S (see their Figure 14). At day 70 the trapped current reaches a maximum speed of 0.35 m s^{-1}, much more intense than their predicted 0.15 m s^{-1} amplitude. Unlike the predictions of Clark and Ahmed, the vertical structure of the alongshore currents in Figure 9 shows a persistent intensification of the alongshore component over the upper continental shelf, with a tendency to extend upward and connect with the surface equatorward jet, all along the coast.

After day 70, the mesoscale cyclonic eddy slowly starts to weaken in strength and extension. By day 85 it almost dissappears from the northern region (Figures 10a and 10c). There is also a weak northward current that strictly follows the coastline, driven by the wind. This partition of the equatorward jet seems to lasts until day 95 (Figures 10b and 10d), when the eddy dissapears and the jet returns to its initial nearshore position. The upwelling activity in the north is stronger than in the south, owing to the fact that there are increasingly strong wind reversals in the south. South of Punta Lavapie the coastal jet gets closer to the coast, and the alongshore current develops subsurface anticyclonic eddies on its offshore side (not shown). These eddies interact with the surface flows, as indicated by intense horizontal density gradients and strong vertical shear of the flows (not shown). Sporadically, anticyclonic eddies are also formed in the offshore side of the jet at the northern regions, along and over the deeper part of the continental slope and over the Peru-Chile Trench.

3.2.4. Coherence Between Winds and Currents. The previous analyses indicate the existence of two distinct dynamical regions, located south and north of Punta Lavapie. To further investigate the mechanism responsible for the differences between those regions, we computed the spectral coherences of time series of "local" winds and alongshore currents. These time series are obtained by averaging the fields over small regions of 50 km×50 km. In these analyses we discriminate among "coastal," "slope," and "trench" regions north and south of Punta Lavapie (thick solid lines in Figure 2). Figure 11 shows that south of Punta Lavapie (at 38°S), alongshore currents and local winds are coherent at the 90% level at periods of ~4 and 9 days. In contrast, there is only weak coherence (≤70%) between local winds and coastal currents in the northern region (at 36°S), indicating that this area is more strongly affected by signals of remote origin. Spectral calculations for slope locations, however, indicate that in the offshore regions the currents and winds are highly coherent, independent of the latitude.

To illustrate the regional differences in the strength of the upwelling activity and its dependence on the local winds, Figure 12 shows the time evolution of local alongshore winds and "middepths" vertical velocities from coastal locations at latitudes 36° and 38°S, smoothed with a second-order low-pass filter (half power cutoff for periods <10 days). The vertical velocities are

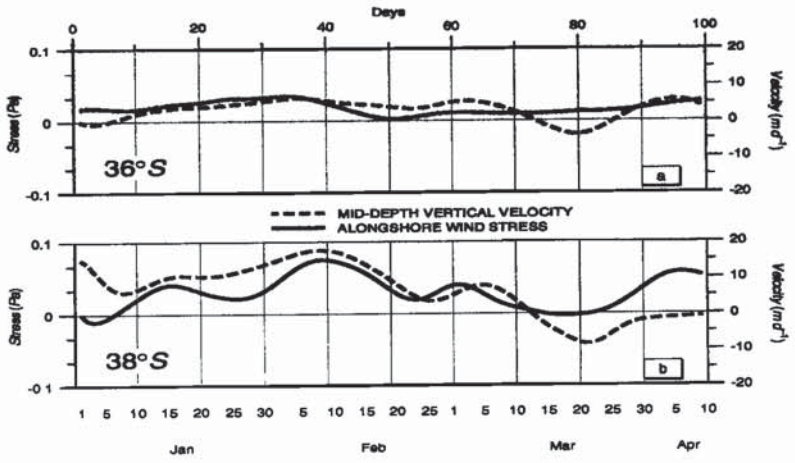

Figure 12. Evolution of local wind stress and "middepths" vertical velocity fields, averaged over regions of 50 km × 50 km centered at coastal locations from latitudes: (a) 36°S and (b) 38°S. The time series have been smoothed with a second-order low-pass filter with a cutoff frequency of 0.1 cpd.

averaged over depths selected to represent the upwelling of subsurface waters. Figure 12 shows that the southern coastal winds and vertical currents (upwelling activity) are stronger and show a general similarity in changes in strength at low frequencies. This is less apparent in the northern locations. Typical "maximum" values of vertical velocity in the southern and northern regions are of ~15 and ~6 m d^{-1}, respectively.

3.2.5. Regional Variability and Wind Forcing. A large part of the variability of the modeled circulation is induced by spatial changes of the wind stress forcing. The southern region is dominated by stronger winds than in the north (Figure 12). To clarify the role played by the variable wind forcing in establishing the regional variability of the ocean fields, we conducted an aditional experiment forced with a uniform and constant wind. The comparison with the the benchmark case is illustrated in Figure 13, where we show surface density maps corresponding to day 100 for both experiments (at this day the observed density differences are the largest, but they are qualitatively valid at any period of the experiments).

The surface density map corresponding to the benchmark case (Figure 13a) shows that the upwelling activity at day 100 has recovered to similar levels of intensity from day 50 (Figure 8b), with dense surface waters extending farther offshore in the north than in the south. This occurs after a strong increase of the upwelling-

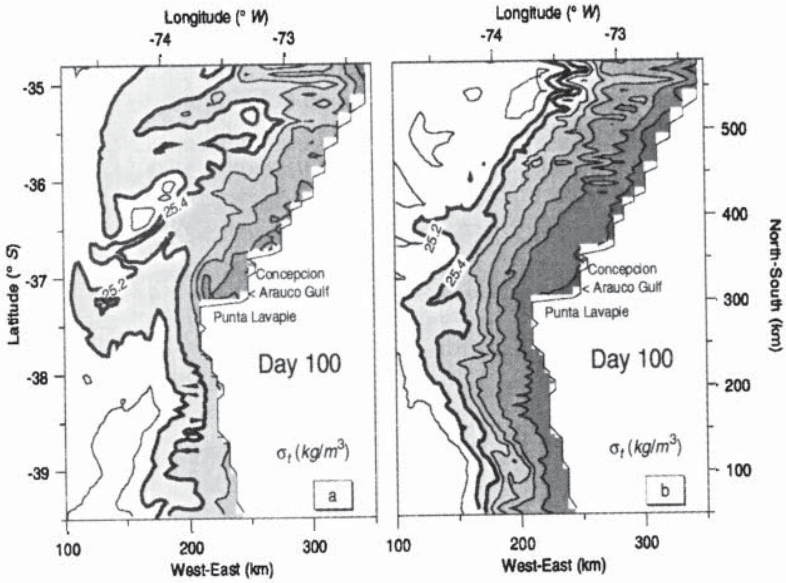

Figure 13. Maps of surface density σ_t at day 100 for experiments (a) benchmark and (b) constant wind=0.1 (Pa). Contour interval is 0.2 kg m^{-3}.

favorable winds (between days 90 and 100). The density map corresponding to a uniform and constant wind (Figure 13b) shows an intensified upwelling activity that reaches farther offshore. In contrast with Figure 13a, the differences between northern and southern coastal density fields are very small, showing the cross-shore variability of the density field as almost uniform along the coast. The barotropic kinetic energy and wind energy inputs of this experiment (not shown) almost double that of the benchmark simulation.

The role of the spatial and temporal variability of the wind forcing is further clarified by comparisons with a numerical simulation made with spatially uniform but time-varying winds. The comparison with the benchmark experiment shows that in the southern regions the model ocean fields caused by spatially uniform, temporally varying winds have characteristics similar to the benchmark. In the northern region, however, the eddy activity during the experiment with spatially uniform winds is significantly weaker (not shown). These results indicate that the regional differences and synoptic fluctuations in the ocean circulation are due to both the spatial and temporal variability of the local wind forcings.

4. Summary and Conclusions

We have presented a numerical study of the upwelling circulation along the central region of the Chilean coast (approximately between 35° and 39°S). The experiment was forced with ECMWF-derived wind stress fields corresponding to the summer of 1993 and heat and salt surface inputs fluxes using a Newtonian damping scheme. Our benchmark results show the formation of an eastern boundary current system that consists of (1) a strong surface equatorward jet (CCC), with oceanic and coastal branches; (2) a weak poleward undercurrent (PUC), below the coastal CCC branch; (3) a strong subsurface equatorward current (SCCC), centered at 1000 m depths over the upper slope; and (4) a deep poleward current (DPC), flowing over the inshore side of the PCT trench. The SCCC and DPC currents are similar to those predicted by *Clark and Ahmed* [1999] and observed by *Shaffer et al.* [1995, 1997], but their existences have not been observationally confirmed for the Gulf of Arauco area. The predicted current system is the result of a wind forcing field that is mostly equatorward and has a dominant cyclonic curl. This wind forcing shows a summer pattern similar to that found by *Bakun and Nelson* [1991], which is determined by changes in the atmospheric Subtropical Anticyclone of the South Pacific.

The coastal areas show strong upwelling activity, induced by offshore Ekman transport, with periods of growth, peak, and decay. These upwelling stages are directly associated with events of intensification or relaxation of the equatorward winds. The changes in the winds and coastline geometry divides the ocean circulation into two distinct dynamical areas that extend north and south of the Punta Lavapie cape, located in the center of the model domain. North of Punta Lavapie the equatorward current separates from the coastline during periods of intensification of the upwelling-favorable winds. During periods of wind relaxation, cyclonic eddies form due to advection from the north. The formation of cyclonic eddies in the northern areas is a recurrent feature that generates strong cross-shelf transport. The topographic mechanism of jet separation is similar to that observed by *Barth et al.* [2000] in the vicinity of Cape Blanco, Oregon. Spectral calculations and sensitivity experiments show that the northern coastal areas are affected more by remote forcing events and less by relatively weaker local winds. In the southern areas, in contrast, the equatorward flows remain persistently attached to the coastline and are highly coherent with relatively stronger local winds.

The analysis of the model fields above indicate that the adjustment by the sea level and currents show a classical Ekman-geostrophic dynamics. At the surface the balance is primarily Ekman dynamics, as the coastal sea level drops due to wind stress and Coriolis forcings. The drop in the coastal sea level results in an across-shelf pressure gradient and an alongshore equatorward coastal jet, as the dynamics of the flows tend to be dominated by geostrophy (with the currents following contours of f/D). Further analysis of the flow adjustment dynamics will be presented in a future article.

Acknowledgments. This work has been supported by NASA grant NAGW-2475, JPL grants 958128 and 1206714, NSF grant 9711344, and ONR grant N14-97-1-0165. We are indebted to M. H. Freilich for providing the ECMWF wind field data.

References

Ahumada, R., Produccion y destino de la masa fitoplanctonica en un sistema de bahias en Chile central: Una hipotesis, *Biol. Pesq., 18,* 53-66, 1989.

Arcos, D., and N. Navarro, Analisis de un indice de surgencia para la zona de Talcahuano, Chile (Lat. 37°S), *Invest. Pesq. Chile, 33,* 91-98, 1986.

Bakun, A., and C. S. Nelson, The seasonal cycle of wind-stress curl in subtropical eastern boundary current regions, *J. Phys. Oceanogr., 21,* 1815-1834, 1991.

Barth, J. A., S. D. Pierce, and R. L. Smith, A separating coastal upwelling jet at Cape Blanco, Oregon and its connection to the California Current System, *Deep Sea Res., 47,* 783-810, 2000.

Batteen, M. L., C.-P. Hu, J. L. Bacon, and C. S. Nelson, A numerical study of the effects of wind forcing on the Chile Current System, *J. Oceanogr., 51,* 585-614, 1995.

Blumberg, A. F., and G. L. Mellor, A description of a three-dimensional coastal ocean circulation model, in *Three-Dimensional Coastal Ocean Models,* Vol. 4, edited by N. Heaps, pp. 1-16, Coastal Estuarine Sci., AGU, Washington D.C., 1987.

Caceres, M., and D. Arcos, Variabilidad en la estructura espacio-temporal de un area de surgencia frente a la costa de Concepcion, Chile, *Invest. Pesq. Chile, 36,* 27-38, 1991.

Clark, A. J., and R. Ahmed, Dynamics of remotely forced intraseasonal oscillations off the western coast of South America, *J. Phys. Oceanogr., 29,* 240-258, 1999.

Djurdfeldt, L., Circulation and mixing in a coastal upwelling embayment: Gulf of Arauco, Chile., *J. Cont. Shelf Res., 9*(II), 1003-1016, 1989.

Enriquez, A. G., and C. A. Friehe, Effects of wind stress and wind stress curl variability on coastal upwelling, *J. Phys. Oceanogr., 25,* 1651-1671, 1995.

Levitus, S., and R. Gelfeld, NODC inventory of physical oceanographic profiles, in *Key to Oceanography Records Documentation 18,* Natl. Oceanic Data Center, Washington, D.C., 1992.

Lonnberg, P., D. Shaw, and P. Unden (Eds.), Research manual 1, ECMWF data assimilation, scientific documentation, Eur. Cent. for Medium-Range Weather Forecasts, Reading, England, 1989.

Matano, R. P., E. D. Palma, J. M. Mesias, and P. T. Strub, Open boundary conditions for use in coastal models, in *Estuarine and Coastal Dynamics,* edited by M. L. Spauling and A. F. Blumberg, pp. 541-555, Am. Soc. Civ. Eng., New York, 1998.

Mellor, G. L., and T. Yamada, Development of a turbulence closure model for geophysical fluid problems, *Rev. Geophys., 20,* 851-875, 1982.

Mellor, G. L., T. Ezer, and L.-Y. Oey, The pressure gradient conundrum of sigma coordinate ocean models, *J. Atmos. Oceanic Tech., 11,* 1126-1134, 1994.

Nuñez, R. H., A study of the ocean circulation off the coast of Chile, *Tech. Rep. 96-4,* 95 pp., COAPS, Fla State Uni., Tallahassee, 1996.

Palma, E. D., and R. P. Matano, On the implementation of open boundary conditions to a general circulation model: The barotropic mode, *J. Geophys. Res., 120,* 200-203, 1998.

Ramage, C. S., El Niño, *Sci. Am.,* Vol. 254, 76-83, 1986.

Rutllant, J., Coastal lows and associated southerly wind events in north-central Chile, paper presented at Fourth International Conference on Southern Hemisphere Meteorology and Oceanography, Am. Meteorol. Soc., Hobart, Australia, 1993.

Shaffer, G., S. Salinas, O. Pizarro, A. Vega, and S. Hormazabal, Currents in the deep ocean off Chile (30°S), *Deep Sea Res., 42,* 425-436, 1995.

Shaffer, G., O. Pizarro, L. Djurfeldt, S. Salinas, and J. Rutllant, Circulation and low-frequency variability near the chilean coast: Remotely forced fluctuations during the 1991-92 El Niño, *J. Phys. Oceanogr., 27,* 217-235, 1997.

Smagorinski, J., General circulation experiments with the primitive equations, I, The basic experiment, *Mon. Weather Rev., 91,* 99-164, 1963.

Strub, P. T., J. M. Mesias, and C. James, Altimeter observations of the Peru-Chile Countercurrent, *Geophys. Res. Lett., 2* (3), 211-214, 1995.

Strub, P. T., J. M. Mesias, V. Montecino, J. Rutllant, and S. Salinas, Coastal ocean circulation off western South America, in *The Sea,* Vol. 11, edited by A. R. Robinson and K. H. Brink, pp. 273-313, J. Wiley & Sons, New York, 1998.

Trenberth, K. E., J. G. Olson, and W. G. Large, A global ocean wind stress climatology based on ECMWF analyses, *Tech. Note NCAR/TN-338+STR,* 93 pp., Natl. Cent. for Atmos. Res., Boulder, Colo., 1989.

Vergara, J., Un modelo numerico bi-dimensional continuamente estratificado para el estudio de la surgencia costera, *Invest. Pesq. Chile, 36,* 39-50, 1991.

Vergara, J., Effects of coastline geometry on wind-induced upwelling in the Chilean coast: A numerical study, paper presented at Fourth International Conference on Southern Hemisphere Meteorology and Oceanography, Am. Meteorol. Soc., Hobart, Australia, 1993.

R. Matano and T. Strub, College of Oceanic and Atmospheric Sciences, Oregon State University, Corvallis, OR 97331, USA. (rmatano@oce.orst.edu; tstrub@oce.orst.edu)

J. Mesias, School for Marine Science and Technology, University of Massachusetts Dartmouth, New Bedford, MA 02744, USA. (jmesias@oce.orst.edu)

(Received September 21, 2000; revised May 11, 2001; accepted June 5, 2001.)